CHARACTERIZING THE THERMAL-INDUCED DISTORTION OF LARGE-SCALE POLYMER COMPOSITE PRINTED STRUCTURES

Tyler Corum[1], Johnna O'Connell[1], James Brackett[1],
Ryan Spencer[1], Ahmed Hassen[2], Chad Duty[1,2]

[1] University of Tennessee
Knoxville, TN

[2] Oak Ridge National Laboratory
Manufacturing Demonstration Facility
Oak Ridge, TN

Abstract

The Big Area Additive Manufacturing (BAAM) system has been used to print large-scale parts, such as automotive structures and molds for tooling, with fiber-reinforced polymer composites. Incorporating reinforcing fibers in printed parts is commonly used to increase stiffness and strength, but it also introduces significant anisotropy in the thermomechanical performance, which can lead to distortion and warping during thermal cycling. Characterizing and understanding how a printed tool distorts is crucial to maintaining tolerances and avoiding part failure. This study uses digital image correlation (DIC) to measure the coefficient of thermal expansion (CTE) of a printed part from room temperature and to a known steady state temperature. The samples were printed with carbon fiber reinforced acrylonitrile butadiene styrene (CF-ABS). Various nozzle geometries were evaluated in this study with the intent of minimizing the thermal-induced distortion experienced by printed parts.

Introduction

Background

Additive Manufacturing (AM) has been a highly researched topic in academia and industry because of its ability to create complex geometries by adding material only where it is needed rather than removing unwanted material. Large-Scale Additive Manufacturing (LSAM) takes this a step further by offering the ability to print large (>1 m^3) structures at high deposition rates (~50 kg/hr). LSAM systems typically use fiber reinforced polymer (FRP) as feedstock material to decrease the coefficient of thermal expansion (CTE) and increase stiffness [1–3]. The lower CTE and increased stiffness also make FRPs a popular material for printed tooling applications. Not only is having a low CTE important but having a CTE mismatch between the tool and the created part may cause the final part to warp and fall outside of tolerances as shown in Figure 1.

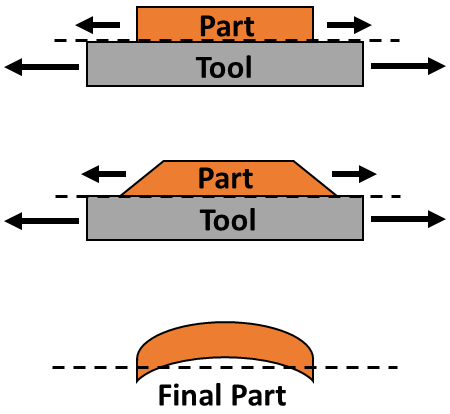

Figure 1. *Mismatch of CTE values leading to part warpage is shown (adapted from [4]).*

While FRP feedstock can reduce CTE compared to the unreinforced "neat" resin, alignment of the fiber reinforcements during the printing process creates a highly anisotropic material. Thermomechanical anisotropy is introduced to the print by the shearing of fibers at the nozzle. The direction of these fibers influences the thermal properties [6–8]. This nozzle shearing causes fiber alignment along the print direction as shown in Figure 2. Fiber alignment caused by nozzle shear force aligns only the outermost fibers of the bead with the direction of the print but leaves the fibers located at the center of the print bead in a random, unaligned orientation [5–7,9]. The fiber alignment along the edge of the bead causes the printed structure to exhibit different CTE values at the edge of a bead compared to the center of the bead [6,7]. The difference in CTE values within each bead creates thermomechanical anisotropy across the entire LSAM structure.

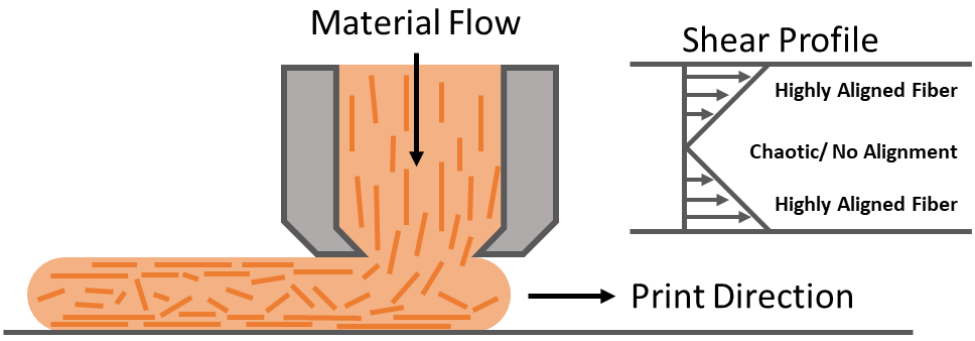

Figure 2. *Fiber alignment due to nozzle shearing is shown above.*

Mechanical anisotropy is also introduced by the hierarchy of the AM process [1,2,10–12]. This is attributed to the layer-by-layer building technique utilized by AM shown in Figure 3. A single bead is extruded in the x-direction and is repeated, bead by bead, until the layer is complete. Layers are completed and build upon each other until the final structure is finished. Mechanical strength along a single bead (x-direction) is higher than across multiple beads (y-direction). Similarly, the strength within a single layer (x,y-direction) is higher than between multiple layers

(z-direction) [1,10]. Other print parameters such as print orientation and raster angle can also effect the mechanical properties of the final part [13–15].

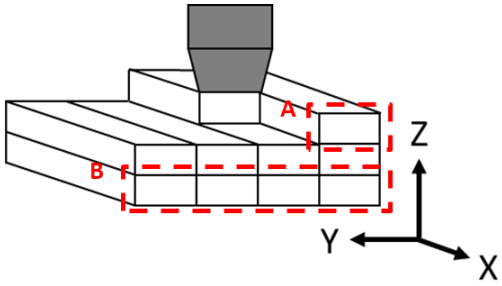

Figure 3. *Print hierarchy is shown above with the print beads (A) and print layers (B).*

Thermomechanical Analysis

CTE is traditionally measured using thermomechanical analysis (TMA). This method relies on heating a sample in a furnace, recording temperature with a thermocouple, and recording the material expansion using a linear variable differential transformer (LVDT) probe. TMA is a reliable and trusted method for measuring the CTE of a homogenous material, however, there are several challenges when applying this technique to LSAM structures. A TMA sample generally has dimensions on the order of 10 x 10 x 10 mm or smaller [16], but a single LSAM bead can have a width of 7 - 15 mm [1,2,7,17]. This size limitation of TMA means that the traditional method cannot accurately represent the large, LASM-printed structure using a single sample. The anisotropy of FRP structures complicate this further with the different thermomechanical properties across a single bead. The limitations faced by TMA suggest that this method is not suitable for LSAM structures and other methods must be explored. Hoskins explored using Digital Image Correlation as an effective method for measuring LSAM samples without the size limitations of TMA [18,19].

2D Digital Image Correlation

A common data collection method that is compatible with large parts is Digital Image Correlation (DIC). This technique is an accurate way to measure the strain of a part by imaging a surface before and after that part undergoes deformation [20–25]. A 2D DIC system uses a camera and computer program to track surface movement as shown in Figure 4. Surface movement is tracked by coating a sample surface in a white background and covering that background with small, black speckles. Once images are taken and compiled, a grid called a subset is imposed over each image. The size of the subset is determined by the user and directly effects the accuracy of the results [22,24,26]. Selecting a subset too small may not provide the computer software with enough unique speckle points to track movement but selecting a subset too large may underestimate the strain experienced by the sample. With the appropriate subset over each image,

the DIC software then compares each image to the first image taken. The first image taken in the set is referred to as the reference image. Comparing each image to the reference image allows the software to record how the position subset changed from the reference image to the current image. Within the subset, each pixel in the image is assigned a numerical value based on the grayscale contrast created by speckling and allows the software to compare position of the subset before and after deformation [20,23,25,26]. A position vector is then calculated from the center of the reference image subset to the center deformed image subset as shown in Figure 5. Each position vector in the image is used to calculate an average strain for that image. This process is repeated for each image until an average strain is determined for the set of images.

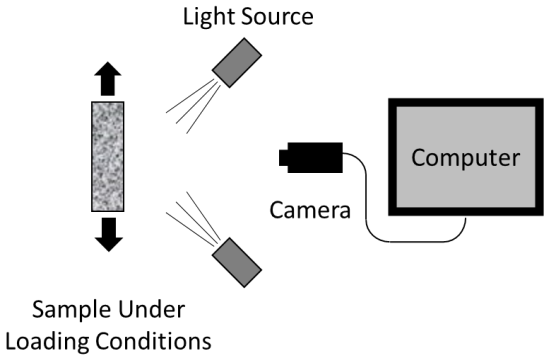

Figure 4. *Typical 2D DIC experimental setup is shown above (adapted from [23]).*

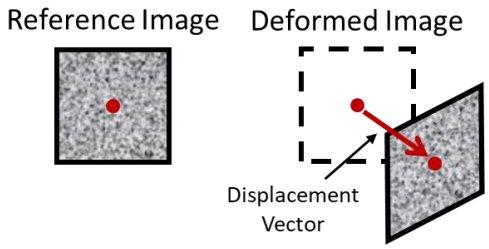

Figure 5. *Subset tracking from the reference to deformed image is shown (adapted from [23]).*

DIC Oven

This research uses DIC to measure the thermal-induced distortion of LSAM structures printed with FRP using a unique DIC Oven setup. This method uses 2D DIC to track the strain experienced by a sample before and after thermal loading. The DIC recorded strain and known furnace temperatures can be used to calculate CTE. This method of measuring CTE is advantageous because it does not face the limitations of TMA. An experimental setup for the system used in this study is shown in Figure 6. Unlike in traditional 2D DIC with the camera horizontal to the sample, this novel setup has the camera placed under the sample. The location of the camera is important to consider when measuring the face of an expanding material. This camera placement minimizes expansion towards the camera from being read falsely as additional

strain experienced by the sample. In this experimental setup, the speckled sample is placed on a fixed sample tray that only allows expansion away from the camera to reduce false strain readings. Initial studies of this novel system have been documented by Hoskins in previous work [18,19]. However, several improvements to the DIC Oven have been made for this study to reduce system noise (random, inaccurate values recorded by the system) and achieve more accurate results.

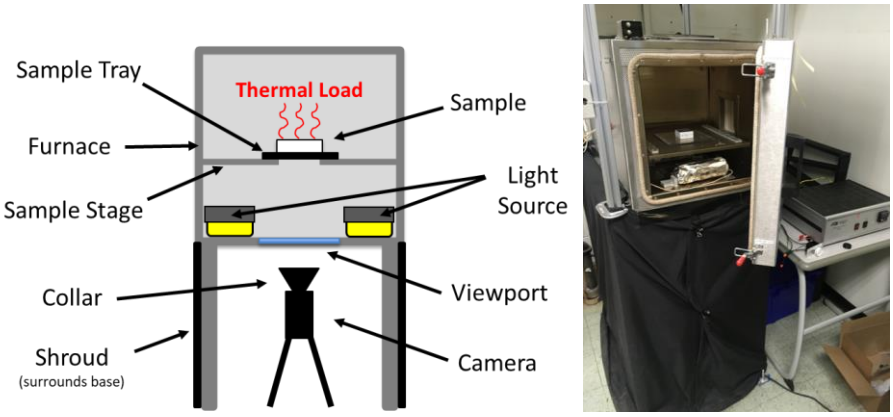

Figure 6. *A diagram (left) of the major components of the DIC Oven (right) is shown.*

System Improvements

Improving the existing system was the first step in accurately measuring CTE of LSAM structures. The DIC Oven has been used in initial studies to measure the CTE of printed parts, but original results exhibited high standard deviations and had not been calibrated relative to a reference sample. This section details efforts to minimize the system noise by various DIC Oven improvements.

Focus and Resolution

Positioning of the camera tripod was the first change to the original setup described by Hoskins [18,19]. The camera was repositioned so that the camera lens was 70 mm from the viewport and 250 mm from the sample. This reduced the amount of dead space in the images captured by the camera and helped the imaged sample maximize the field of view (FOV). With the new camera position established, the lens was refocused to improve image resolution, which allows the DIC computer software to more accurately track speckle location before and after distortion [21]. Figure 7 demonstrates the improved pixel resolution obtained by repositioning the camera. The 40 x 40 mm images shown in Figure 7 are the same sample, speckle pattern, and dimensions. The only difference in these images is the described changes in camera position and focus. The 2.5 x 2.5 mm images in Figure 7 show a zoomed in region with highlighted areas comparing the improvement in clarity from the left to the right image. Notice that in the before 2.5 x 2.5 mm image that this was the maximum zoom of the system. Maximum zoom after the

improvements were made is also shown by the far right 0.81 x 0.81 mm image of Figure 7. This new maximum zoom demonstrates how clearly and precisely the camera can image each speckle, which was quantified by an increased in pixel resolution from 60 microns/pixel to 28 microns/pixel.

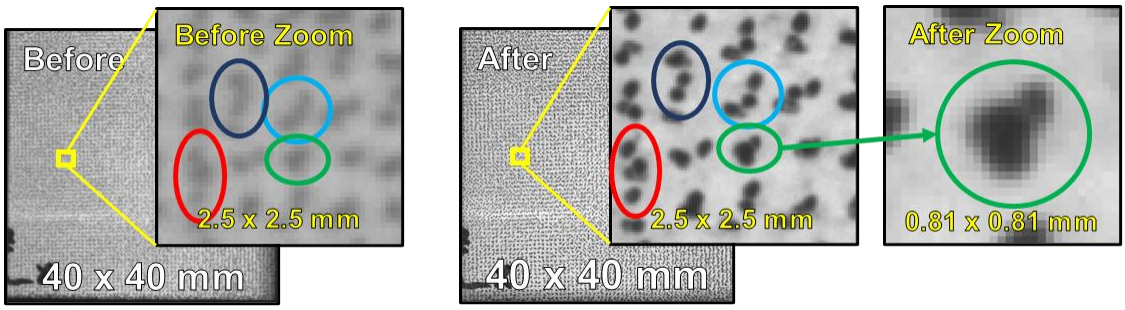

Figure 7. *Above shows the progression of the camera resolution before (left image set) and after (right image set) adjustments were made.*

Glare Reduction

Glare from light entering the system and reflecting off floor tiles onto the bottom viewport during imaging as a reflection of the camera was also found to contribute to system noise. This glare reflection picked up by the camera is shown on the left side of Figure 8. To minimize this glare and get a more consistent image, the "Collar" was created and added to the camera lens. The collar, shown in Figure 8, is a retrofit design made to fit the existing camera and block out any excess light or small particles that may interfere with the camera lens during imaging. The collar was modeled using SolidWorks and created using a fused filament fabrication (FFF) 3D printer. Once created and slightly adjusted to fit the existing camera lens, the collar was coated in a thin layer of Rust-Oleum High Temperature spray paint with a matte black finish to cover any existing sheen from the filament. Adding the collar significantly minimized glare seen by the camera, as shown by Figure 8, and provided the DIC computer software with a clearer, more consistent image.

Figure 8. *An image before (left) and after (right) the collar was added that shows significant glare reduction.*

Lighting

The system lighting was also changed to evenly illuminate the sample. The original lighting within the furnace was a light bulb on opposite sides of the sample with a dimmer switch to adjust brightness. Lighting the entire furnace caused bright spots on either side of the sample from the lightbulbs themselves or from light reflecting off the stainless-steel walls inside the oven. Since photographers use indirect lighting to avoid taking an unevenly illuminated picture, the same logic was applied to the DIC Oven by adding angled light diffusers (ALDs) to the existing light sources. The ALDs are shown in Figure 9 and are constructed of aluminum foil, parchment paper, and staples. This specific construction allows the ALDs to withstand the high temperatures in the DIC Oven without combusting or deforming. The diffusers help to light the inside of the furnace more evenly. Angling these diffusers allows the light to bounce off the bottom face of the furnace and indirectly light the sample as shown in Figure 9. The ALDs are also capped at both ends in aluminum foil to prevent light from bouncing off walls perpendicular to the light source. Figure 10 provides an example of how the change in lighting approach led to more consistent results from the DIC process.

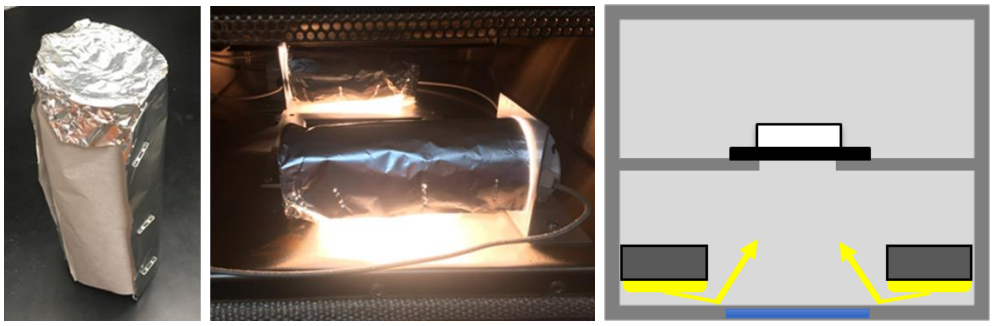

Figure 9. *Shown above is the angled light diffusers (left and middle) and a lighting diagram of the furnace (right).*

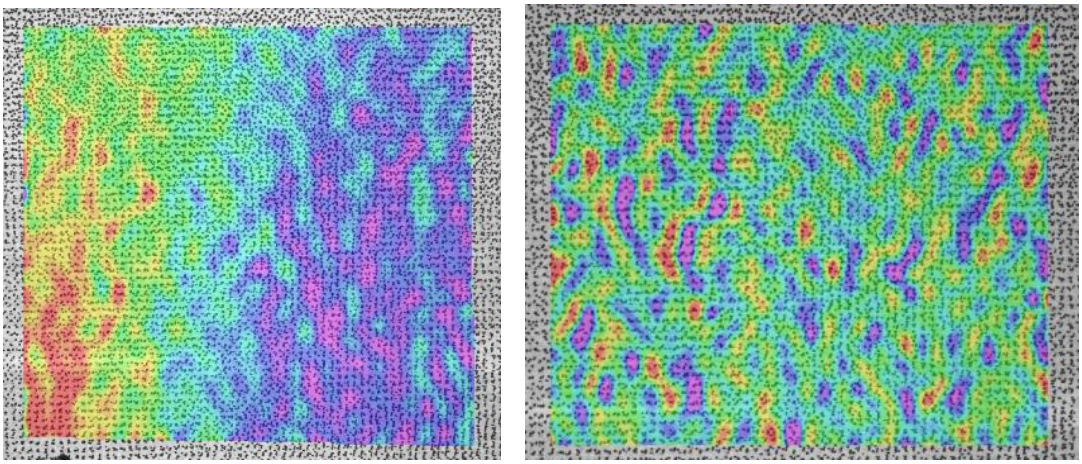

Figure 10. *An image taken before (right) and after (left) the ALDs were put into place.*

Miscellaneous Improvements

The furnace of the DIC Oven came standard with a viewport on the bottom and side. The side viewport of the furnace was covered by a sheet of aluminum to avoid any unwanted light in the system. The glass pane used in the viewport on the bottom of the DIC Oven was removed and replaced with quartz glass. Quartz glass is of better quality than standard glass and reduces the error caused by the inconsistent thickness and refraction of standard glass pane [20,22]. The shroud that surrounds the oven base, as shown by Figure 6, was redesigned so that it attached to each corner of the oven base by a small c-clamps, and the sides were lined with adhesive tape to create a permanent seal to prevent light from entering the system. The design described by Hoskins included small dampeners located under each corner of the sample stage with intensions to further minimize vibrations [18,19]. However, this study found these dampeners had a CTE value of 345.3 μm/m°C and were removed to avoid any drastic expansion during DIC Oven imaging.

Image Coverage and Count

Additional changes were made to the existing procedure to further reduce system noise. Speckle size and coverage is the key to tracking the position of subsets and will affect the accuracy of DIC measurements [22–24]. Speckles that are too large or too dense will not provide enough data points to the DIC software, while speckles too small or too sparse may not be unique enough to have the position recorded accurately. Room temperature tests were run with different speckle size and coverage since any strain at room temperature should equal zero. This meant results that minimized room temperature strain were most accurate. It was determined that a 0.007” dot size that covered the sample with six passes by the Correlation Solutions Speckle Kit stamp provided contrast with the least system noise.

The next step was validating the number of images necessary per image set to record all surface movement with the improved speckle coverage and pixel resolution. An image trial was performed at room temperature using 5 different samples to determine how many images were required in each image set to accurately represent the average strain experienced by a sample. Results of this trial are shown in Figure 11 where the x-direction continuous strain average (top plot) for each sample tested as well as the change in the continuous strain average (bottom plot) from the previous image. Only the x-direction values were presented because these values were ~10 times smaller than associated z-direction counterparts. The average strain of each image stabilized near image 22 for all 5 samples tested, suggesting that image 22 accurately captured the average strain experienced by each sample. This was further reinforced by the change in continuous strain plot that shows 97% of data points recorded after image 22 were within 0.1% change from the previous image. With 22 images accurately capturing the average strain of the image set, more than doubling the number of images taken to 45 will accurately capture the surface movement of the sample.

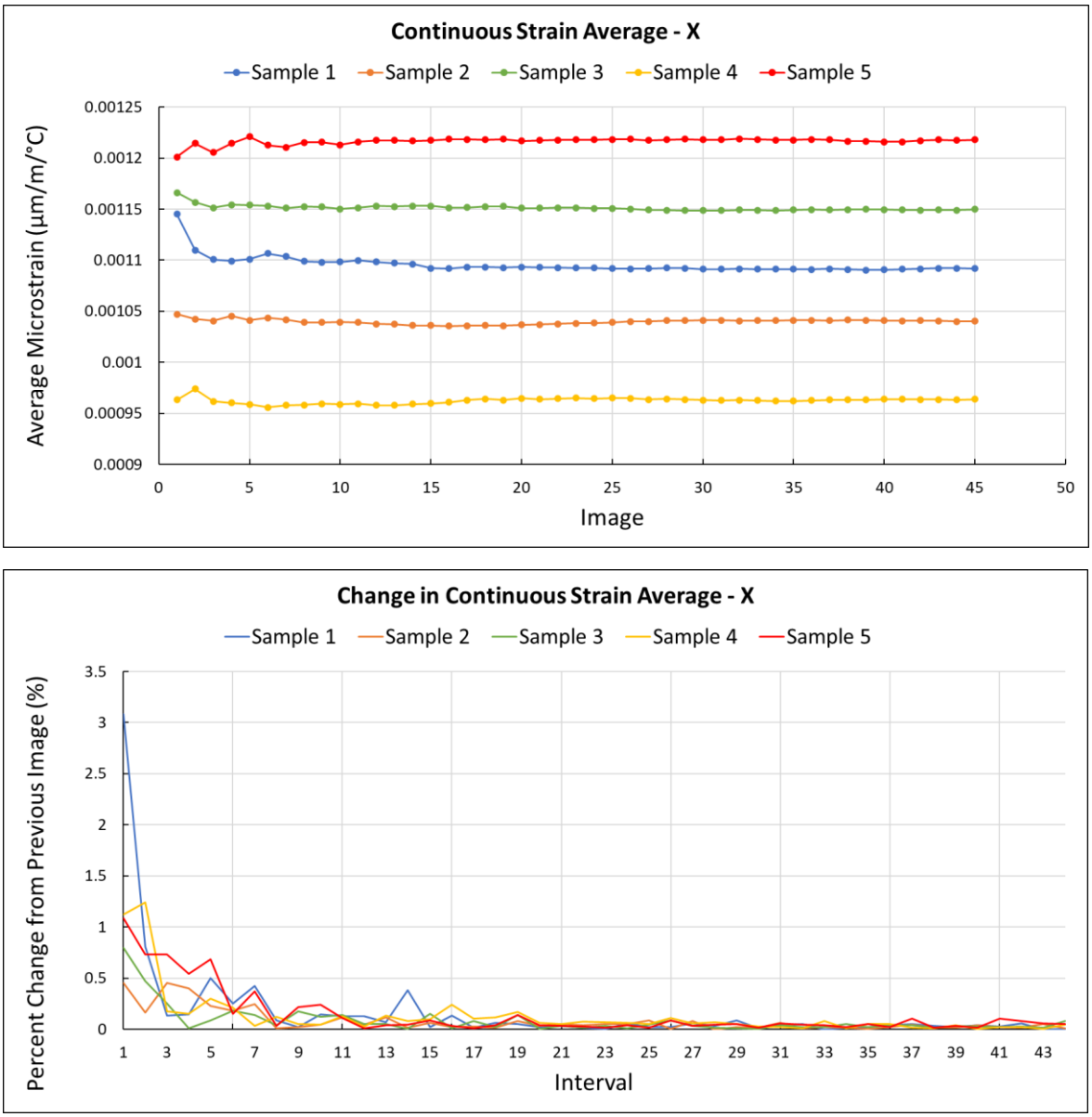

Figure 11. *The Continuous Strain Average (top) and Change in Continuous Strain Average (bottom) show that 45 images are enough to accurately capture strain experienced by a sample.*

Validation of System Improvements

Data showed reduced system noise after the improvements were implemented, and the impact of these changes are illustrated by the figures below. Images of the same speckled sample were captured at room temperature before and after any improvements were made. Vic-2D was used to create a 2D strain map of the before and after image set. These strain maps are shown in Figure 12. Since these images were taken at room temperature, the measured strain should be equal to zero. The before map shows that the system recorded a random spread of strain with a range of 365 microstrain to -1623 microstrain. Each image of the before image set was examined

with no indication of a pattern present. The after image of Figure 12 shows a more homogeneous spread of noise with an order of magnitude lower range of 182 microstrain to -186 microstrain. This remaining strain seen at room temperature by the system was considered general system noise that could be removed during post-processing of the acquired data. The minimized system noise was represented further by a graph that describes the microstrain recorded for each image at room temperature. Figure 13 shows the microstrain measured at room temperature for images captured before and after system upgrades. This chart shows the range of system noise was reduced by 96% and room temperature strain is now centered around zero as expected.

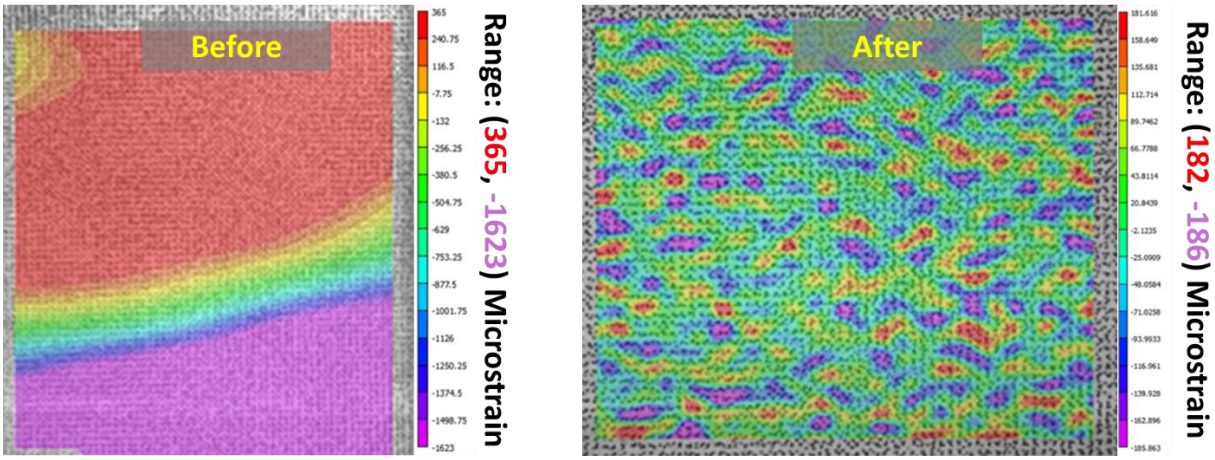

Figure 12. *The room temperature 2D strain maps above show reduced noise and range from before (left) to after (right) the system was upgraded.*

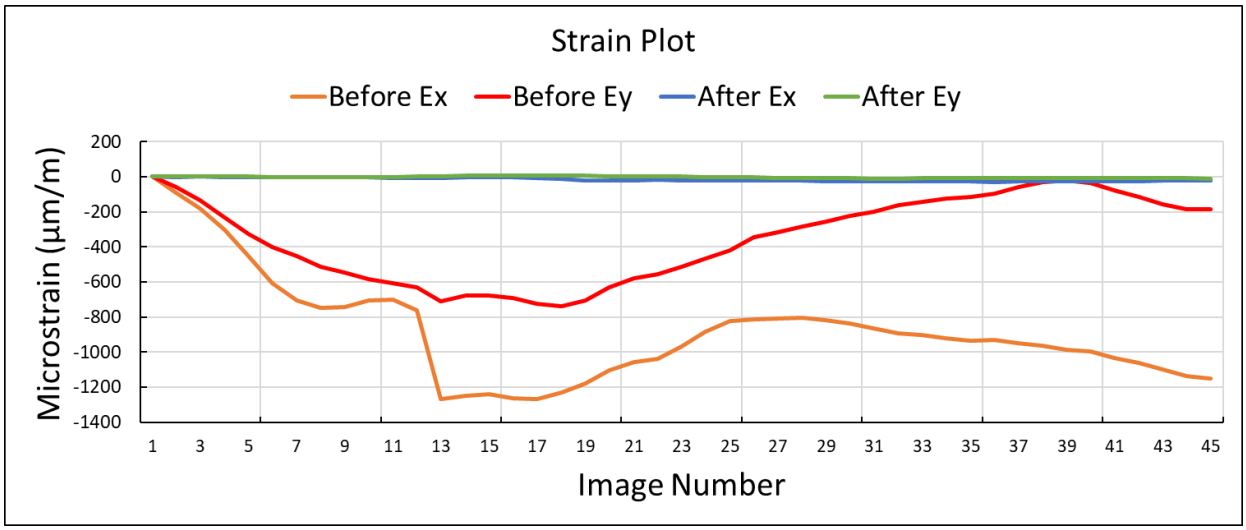

Figure 13. *Shown above is a graph depicting room temperature strain recorded before and after improvements were put into place.*

Calibration

Following system improvements, the DIC Oven was calibrated to quantify accuracy and precision. The reference material chosen was 6061 Aluminum due to its homogeneity, defined CTE value, and the usage of aluminum as a calibration material for TMA systems [27]. Samples were taken from the center of a large aluminum cube (100 x 100 x 100 mm) to avoid any pre-stressed areas from the edges due to the material extrusion process. A TA Instruments Q400 TMA sample (10 x 10 x 8 mm) was taken to represent the x-direction with another sample of the same dimensions to represent y-direction. A 20 mm slice of an xy face was also taken near the center of the cube for the DIC Oven, giving a 50 x 50 x 20 mm block that was spray painted white and speckled. The TMA values were treated as the target values for this calibration given the homogenous reference material and trusted TMA method for this application. Table 1 shows the resulting CTE values of the aluminum calibration from each measurement method. Each calibration sample was measured three times to track the accuracy and precision of the DIC Oven system against the TMA. The three runs for each sample were then averaged and the standard deviation was calculated for each direction of each method.

Table 1. *Calibration results are provided for the DIC Oven.*

Aluminum Calibration CTE Results (µm/m°C)				
	TMA Measurement		***DIC Oven Measurement***	
	x-direction	*y-direction*	*x-direction*	*y-direction*
Run 1	24.0	23.8	23.5	23.9
Run 2	22.6	23.2	23.5	24.1
Run 3	22.6	23.3	23.8	24.4
Avg	**23.0**	**23.5**	**23.6**	**24.1**
Stn Dev	**±0.823**	**±0.329**	**±0.168**	**±0.259**

Calibration results show that the DIC Oven produced similar results to TMA measurements. The average CTE of both systems is higher in the y-direction than in the x-direction. The average CTE recorded by the DIC Oven was within 1.0 µm/m°C of TMA for both the x and y-direction. The standard deviation of the DIC Oven was less than ±0.30 µm/m°C for both directions measured, which was lower than that measured by TMA. Results of the aluminum calibration suggest that the DIC Oven data represents the true CTE of samples.

Experimental Methods

Sample Preparation

The LSAM samples measured in this work were created using Big Area Additive Manufacturing (BAAM) using FRP feedstock [1,2]. There were 10 samples printed using BAAM made of 20% by weight acrylonitrile butadiene styrene (20% CF-ABS) that were prepped for measurement using the DIC Oven. There were 5 nozzle designs (standard and Design A-D) used to create these samples, and each design was used to print two samples for DIC Oven testing. The

objective of each nozzle design was to slightly vary the orientation and distribution of fibers to create a different fiber alignment using each nozzle, but the specifics of each nozzle design are currently proprietary. All samples were dried at 60°C for at least 6 hours. The samples were allowed to cool for at least 2 hours in a desiccator before speckling. Each sample was inspected so that the xy and xz faces with the least defects were selected for DIC. Having a parallel, defect-free face, is crucial for accurate DIC measurement [23]. The selected xy and xz faces were painted white using matte finish Rust-Oleum High Temperature spray paint. Best practice is to use as little spray paint as possible for the white background to avoid tracking the movement of the paint film rather than the sample surface itself [20]. Once the white background was dried, the black speckles were applied using the Correlated Solutions Speckle Kit. The 0.007" dot size was used in this study and each sample was coated in speckles 6 times for adequate coverage, as shown by the speckled sample in Figure 14. This speckle coverage was done for each xy and xz face of interest. TMA samples were also used in this study to compare methods. TMA samples were taken from the same printed parts and tested under the same parameters as DIC Oven samples. The TMA samples were 5 x 5 x 5 mm sections taken from the outer edge and the center of a single bead to provide a CTE value for each sample using both TMA and the DIC Oven.

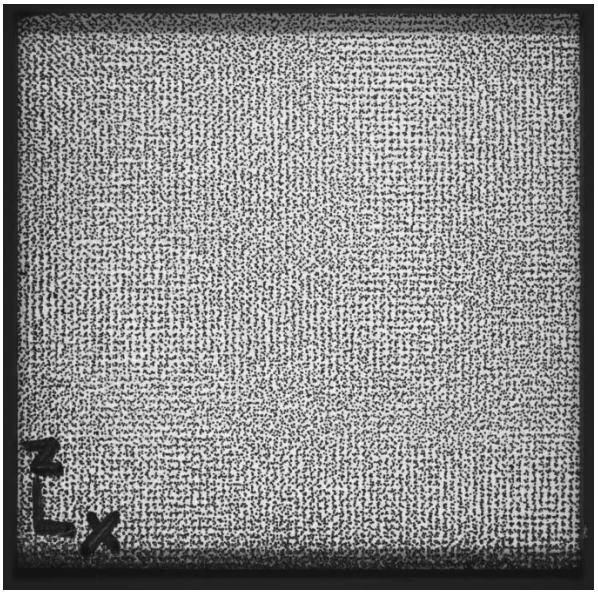

Figure 14. *An image of a fully prepped sample is shown.*

Test Procedure

The DIC Oven was used to measure the CTE values of each CF-ABS sample. Testing began by allowing the Correlated Solutions camera under the furnace to warm up for 10 minutes. A single sample was aligned on the sample tray as parallel as possible so that the x-direction of the physical sample was aligned parallel to the x-direction of the software. Lighting was adjusted so that the sample was lit enough for the camera to image the sample but not so bright that there

was a glare on the sample. Once the sample was properly aligned, brightness was set, and the camera was warmed up, the Vic-Snap software could be used to capture images of the sample. The room temperature was recorded, and a 45-image set was captured at room temperature at intervals of 100 ms. The furnace was then set to a temperature of 90°C and allowed to reach steady state for 6 hours. After the sample reached steady state, the camera was warmed up for another 10 minutes, and a second set of 45 images were taken at the steady state temperature of 90°C.

Vic-2D was used to compile the 90 total images and determine the average strain value of each image using the DIC methods discussed earlier in the work. With the average strain known for each image, an average strain can be calculated for room temperature (ε_{RT}) and steady state temperature (ε_{SS}). Using the known conditions at room temperature (T_{RT}) and at steady state temperature (T_{ss}), the CTE of each sample could be calculated using equation 1. Any room temperature strain should equal zero and was treated as general system noise. Room temperature strain was subtracted from the steady state strain for this reason.

$$CTE = \frac{\varepsilon_{SS} - \varepsilon_{RT}}{T_{ss} - T_{RT}} \qquad (1)$$

Once all 10 samples were tested in the DIC Oven, the procedure was repeated with a "flipped" sample. Flipped samples were adjusted so that the x-direction of the physical sample was perpendicular to the x-direction of the software. This step was taken to minimize any possible biasing from lighting or from the sample alignment process. The flipped sample alignment was the only alteration to the procedure with all remaining steps repeated. The flipped orientation and normal orientation CTE values were averaged together based on the physical sample directions to determine a final CTE value of each sample for the x, y, and z-directions. The standard deviation of the CTE values was also calculated for each sample.

The average CTE values measured by the DIC Oven were plotted for each direction. TMA data of the same sample was imposed over the DIC Oven values to directly compare methods. The TMA data was left as inner and outer bead values to compare CTE location to the average value measured using the DIC Oven. Since maintaining orthotropic properties is an important aspect for tooling applications and a driving force in this study the orthotropic ratios of the different nozzle designs were compared to that of the standard nozzle. This was done by dividing the y-direction CTE by the x-direction CTE and was repeated for z divided by x. Normalizing each direction by x helped to better characterize orthotropic properties based on fiber alignment from different nozzle design.

Results and Discussion

The CTE values measured by the DIC Oven for each sample are discussed as well as the importance of these results with respect to tooling. There were 10 FRP samples testing using the DIC Oven. Sample sets were averaged to give a CTE experienced by the CF-ABS based on the

nozzle used during printing. The data discussed in this section represents how CTE values of the samples were affected nozzle designs A-D compared to the standard nozzle to better determine how different fiber alignment effected the CTE.

Standard Nozzle

The CTE values in the x, y, and z-directions for the standard nozzle are shown in Figure 15. The trend of CTE data increasing from the x to the z-direction was expected due to fiber alignment. The x-direction saw the lowest CTE because the fibers were most aligned in this direction and minimized the thermal expansion along fibers. The y-direction experienced high CTE due to the chaotic distribution of fibers allowing higher expansion across beads. The z-direction CTE was highest from both chaotically distributed fibers and weak bonds between layers. The standard deviation of the x, y, and z-direction CTE for the standard nozzle was low. TMA data from the same print was imposed over the DIC Oven data for a comparison between the two methods. CTE values calculated using TMA were taken from the inner and outer portion of the bead for each direction. Notice that the DIC Oven data falls within one standard deviation of the CTE values calculated using TMA.

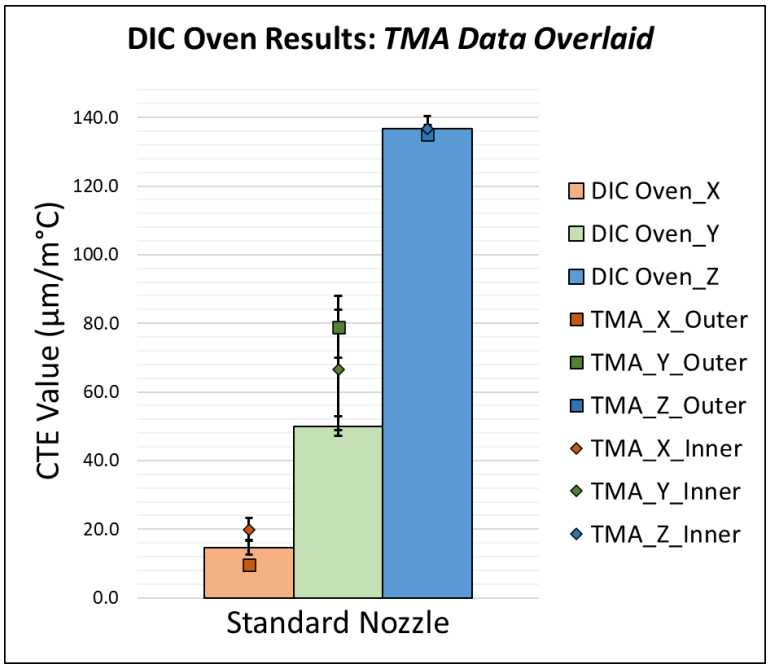

Figure 15. *The CTE values of the standard nozzle are shown above with TMA values overlaid for comparison.*

The orthotropic ratios for each nozzle are represented in this study by comparing CTE values between different directions. Figure 16 represents orthotropic properties of the standard

nozzle by normalizing CTE measured in the y and z-direction to the CTE measured in the x-direction. Perfectly orthotropic properties would be represented in Figure 16 as a value of 1. The value of 3.41 for the y-direction represents that the CTE experienced in the y-direction is 3.41 times higher than the CTE measured in the x-direction. The standard nozzle produced samples with less orthotropic properties in the z-direction than in the y-direction.

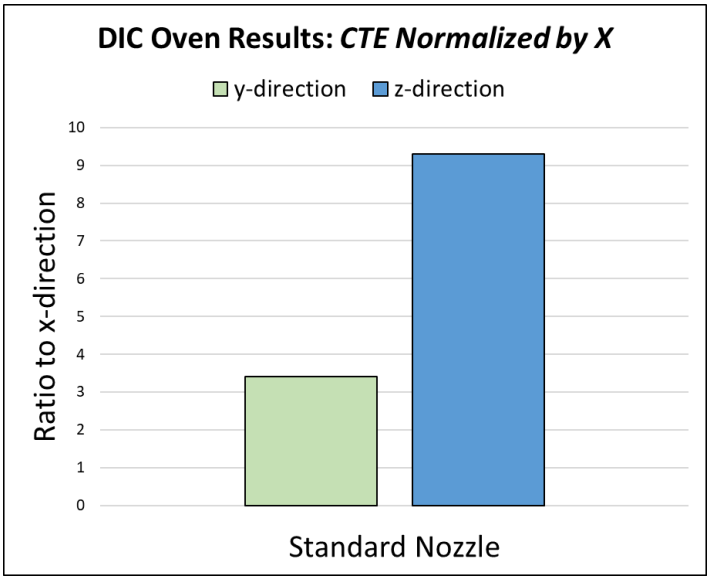

Figure 16. *CTE ratios normalized by the x-direction are shown for the standard nozzle.*

Nozzle Designs A, B, C, and D

The CTE relationship of each nozzle design between the DIC Oven and TMA are shown in Figure 17. There were no CTE values provided by Figure 17 to protect proprietary data, but the similarities between the DIC Oven and TMA on the CTE values can be shown and discussed relative to each other. There was no TMA data provided for Design C due to poor surface finish of the printed part. The CTE data collected follows the same expected trend of values increasing from x to z-direction as a result of fiber alignment due to nozzle shear. Notice that most DIC Oven measurements fall within one standard deviation of the TMA values. The only value not in this one standard deviation range, Design A's z-direction, is close to having the standard deviations overlap. Further, Figure 17 also shows several instances where DIC Oven results fall between the TMA inner and outer bead values. In other cases, the DIC Oven results were more similar to either the inner or outer value, reinforcing that TMA does not always accurately represent a LSAM sample just by averaging the inner and outer bead CTE values.

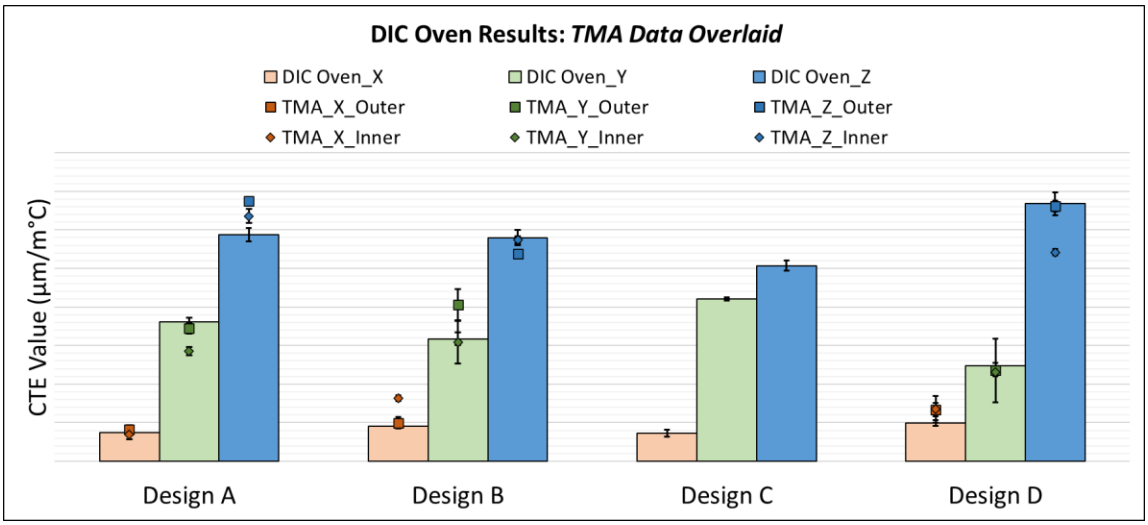

Figure 17. *The CTE values of the different nozzle designs are shown above with TMA values overlaid for comparison.*

Orthotropic properties of the different nozzle designs are shown in Figure 18. The orthotropic properties in the z-direction were improved by designs A-D when compared to the standard nozzle, however, all but one of the y-direction ratios were increased rather than decreased. These results indicate that orthotropic CTE properties can be influenced by nozzle design, and for this study, Design D provided the greatest improvement in orthotropic properties. Unlike the other three designs, Design D was able to improve orthotropic properties by lowering both the y and z-direction CTE ratios.

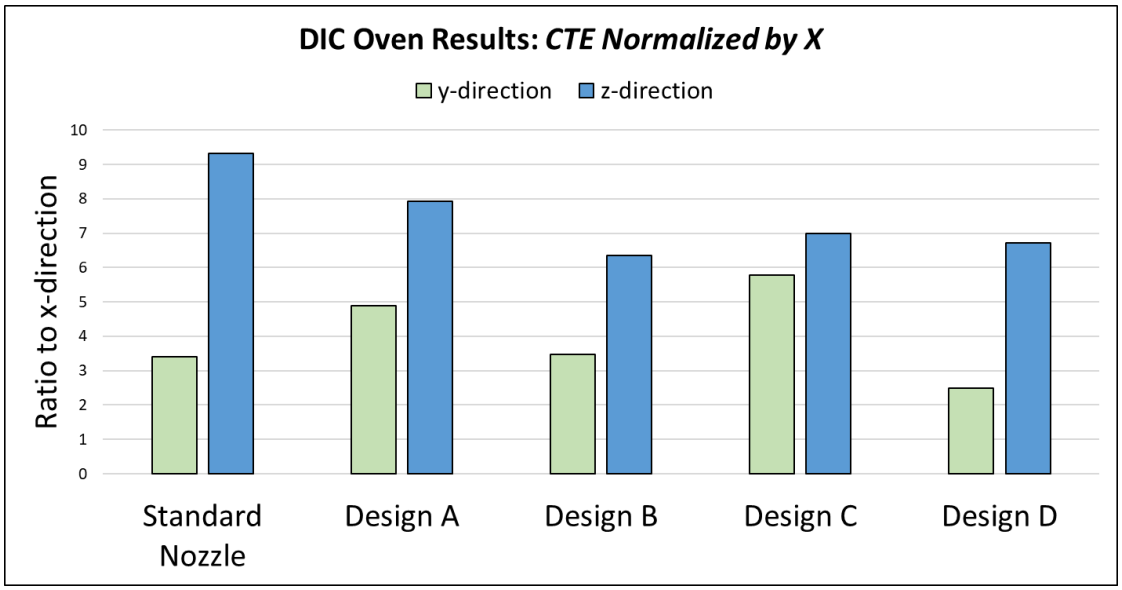

Figure 18. *CTE ratios normalized by the x-direction are shown for each nozzle.*

Relating Sample Properties to Structure

Vic-2D was used to create the strain maps shown in Figures 19 and 20. These 2D strain maps show a clear relationship between the properties of the structure and how the sample was printed. Figure 19 shows the xy-plane strain with homogeneous spread of low strain in the x-direction and a very defined purple strain in the y-direction. There is a clear interaction between the beads on the top surface of the sample shown by the strain map. This was expected from fibers at the edge of the bead being aligned due to nozzle shearing. This purple strain line is a negative strain with high strain on either side of that line. This was interpreted as the bead interaction attempting to hold the structure together while the beads were clearly attempting to expand. The xy-plane results could differ when using a larger sample that captures more bead interactions. Figure 20 shows the xz-plane strain map. The xz-plane also saw a low strain value throughout the x-direction with very high, defined sections of red strain in the z-direction. The red lines in the z-direction represent high points of strain between print layers. These were expected results from fiber alignment occurring at the nozzle to better orient fibers. This led to more stress experienced between layers. The 2D strain maps show clearly that there is a correlation between the sample properties and how the samples were printed.

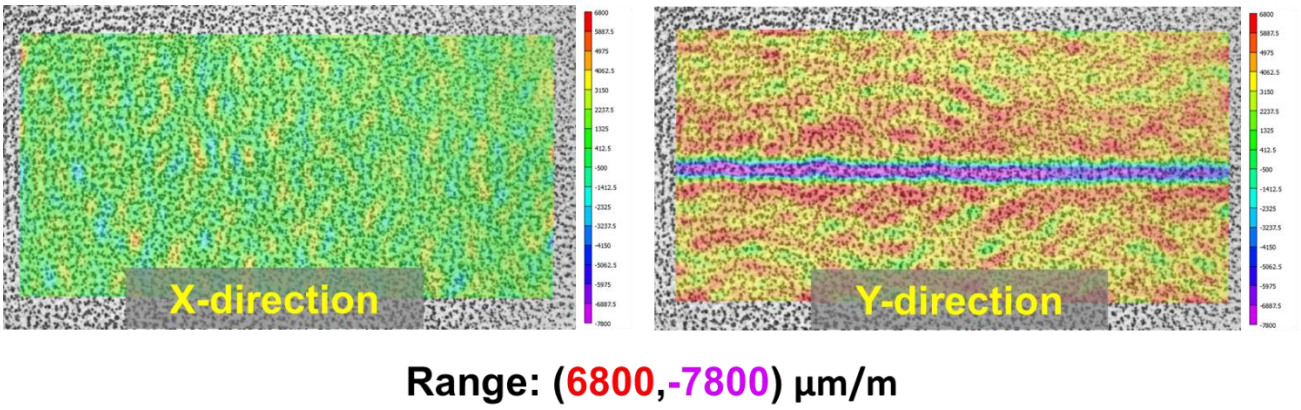

Figure 19. *The 2D Strain map for the XY plane is shown with a color scale for reference.*

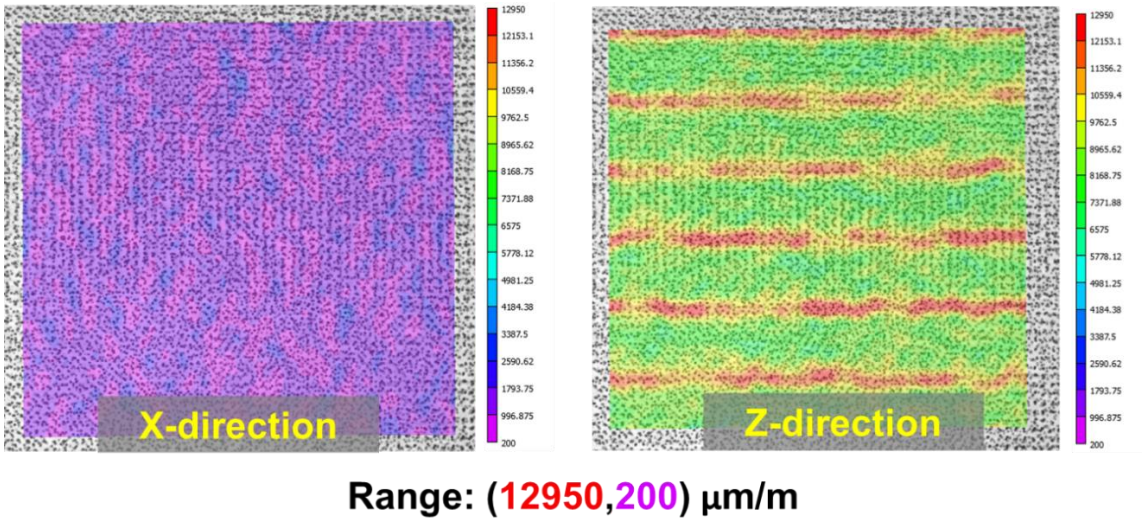

Figure 20. *The 2D Strain map for the XZ plane is shown with a color scale for reference.*

Conclusions and Future Work

The objective of this study was to improve the DIC Oven system and validate a method of measuring the CTE of LSAM structures. TMA is traditionally used to calculate CTE but has limited value when using large, anisotropic structures. The DIC Oven system was modified to accurately track surface movements of large AM samples as a function of temperature. Significant improvements to the system reduced the noise level by 96 %, and the DIC Oven was calibrated to within 20 ppm accuracy using a known, homogenous reference material. The improved system was then used to characterize CF-ABS samples printed using BAAM with five different nozzle design. The CTE values from the DIC Oven were comparable to values collected using TMA taken from sections of the same print. As expected, the measured CTE values of the standard nozzle showed that the y and z-direction CTE were very different. More importantly, changing nozzle design to alter shear occurring in the nozzle successfully influenced the CTE of printed samples. Each design was able to decrease z-direction CTE, but only Design D was able to lower the CTE in both the y and z-direction. For large-scale printed samples, the DIC Oven provides a more accurate method of measuring CTE of LSAM structures than TMA as represented by the 2D strain maps that relate properties of the sample to the structure of the sample. Future work will focus on developing a method to predict the CTE of LSAM structures that enables part designs to reach correct dimensions after thermal-induced distortion occurs.

Acknowledgements

This research was funded by the Southeastern Advanced Machine Tools Network (SEAMTN) at the University of Tennessee, Knoxville and sponsored by the U.S. Department of Energy, Office of Energy Efficiency and Renewable Energy, Advanced Manufacturing Office, under contract DE-AC05-00OR22725 with UT-Battelle, LLC.

References

[1] C.E. Duty, V. Kunc, B. Compton, B. Post, D. Erdman, R. Smith, R. Lind, P. Lloyd, L. Love, Structure and mechanical behavior of Big Area Additive Manufacturing (BAAM) materials, Rapid Prototyp. J. 23 (2017) 181–189. https://doi.org/10.1108/RPJ-12-2015-0183.

[2] C.E. Duty, T. Drye, A. Franc, Material Development for Tooling Applications Using Big Area Additive Manufacturing (BAAM), 2015. https://doi.org/10.2172/1209207.

[3] L.J. Love, V. Kunc, O. Rios, C.E. Duty, A.M. Elliott, B.K. Post, R.J. Smith, C.A. Blue, The importance of carbon fiber to polymer additive manufacturing, J. Mater. Res. 29 (2014) 1893–1898. https://doi.org/10.1557/jmr.2014.212.

[4] G. Twigg, A. Poursartip, G. Fernlund, Tool–part interaction in composites processing. Part I: experimental investigation and analytical model, Compos. Part Appl. Sci. Manuf. 35 (2004) 121–133. https://doi.org/10.1016/S1359-835X(03)00131-3.

[5] H.L. Tekinalp, V. Kunc, G.M. Velez-Garcia, C.E. Duty, L.J. Love, A.K. Naskar, C.A. Blue, S. Ozcan, Highly oriented carbon fiber–polymer composites via additive manufacturing, Compos. Sci. Technol. 105 (2014) 144–150. https://doi.org/10.1016/j.compscitech.2014.10.009.

[6] J.L. Colón Quintana, L. Slattery, J. Pinkham, J. Keaton, R.A. Lopez-Anido, K. Sharp, Effects of Fiber Orientation on the Coefficient of Thermal Expansion of Fiber-Filled Polymer Systems in Large Format Polymer Extrusion-Based Additive Manufacturing, Materials. 15 (2022) 2764. https://doi.org/10.3390/ma15082764.

[7] A.A. Hassen, R.B. Dinwiddie, S. Kim, H.L. Tekinap, V. Kumar, J. Lindahl, P. Yeole, C. Duty, U. Vaidya, H. Wang, V. Kunc, Anisotropic thermal behavior of extrusion-based large scale additively manufactured carbon-fiber reinforced thermoplastic structures, Polym. Compos. 43 (2022) 3678–3690. https://doi.org/10.1002/pc.26645.

[8] P. Roozbehjavan, B. Tavakol, A. Ahmed, H. Koushyar, R. Das, R. Joven, B. Minaie, Experimental and numerical study of distortion in flat, L-shaped, and U-shaped carbon fiber–epoxy composite parts, J. Appl. Polym. Sci. 131 (2014). https://doi.org/10.1002/app.40439.

[9] B. Brenken, E. Barocio, A. Favaloro, V. Kunc, R.B. Pipes, Fused filament fabrication of fiber-reinforced polymers: A review, Addit. Manuf. 21 (2018) 1–16. https://doi.org/10.1016/j.addma.2018.01.002.

[10] C. Duty, J. Failla, S. Kim, T. Smith, J. Lindahl, V. Kunc, Z-Pinning approach for 3D printing mechanically isotropic materials, Addit. Manuf. 27 (2019) 175–184. https://doi.org/10.1016/j.addma.2019.03.007.

[11] D. Jiang, D.E. Smith, Anisotropic mechanical properties of oriented carbon fiber filled polymer composites produced with fused filament fabrication, Addit. Manuf. 18 (2017) 84–94. https://doi.org/10.1016/j.addma.2017.08.006.

[12] F. Ning, W. Cong, Z. Hu, K. Huang, Additive manufacturing of thermoplastic matrix composites using fused deposition modeling: A comparison of two reinforcements, J. Compos. Mater. 51 (2017) 3733–3742. https://doi.org/10.1177/0021998317692659.

[13] S. Ahn, M. Montero, D. Odell, S. Roundy, P.K. Wright, Anisotropic material properties of fused deposition modeling ABS, Rapid Prototyp. J. 8 (2002) 248–257. https://doi.org/10.1108/13552540210441166.

[14] H. Rezayat, W. Zhou, A. Siriruk, D. Penumadu, S.S. Babu, Structure–mechanical property relationship in fused deposition modelling, Mater. Sci. Technol. 31 (2015) 895–903. https://doi.org/10.1179/1743284715Y.0000000010.
[15] R.J. Zaldivar, D.B. Witkin, T. McLouth, D.N. Patel, K. Schmitt, J.P. Nokes, Influence of processing and orientation print effects on the mechanical and thermal behavior of 3D-Printed ULTEM® 9085 Material, Addit. Manuf. 13 (2017) 71–80. https://doi.org/10.1016/j.addma.2016.11.007.
[16] E37 Committee, Test Method for Linear Thermal Expansion of Solid Materials by Thermomechanical Analysis, ASTM International, n.d. https://doi.org/10.1520/E0831-19.
[17] J. Brackett, Y. Yan, D. Cauthen, V. Kishore, J. Lindahl, T. Smith, Z. Sudbury, H. Ning, V. Kunc, C. Duty, Characterizing material transitions in large-scale Additive Manufacturing, Addit. Manuf. 38 (2021) 101750. https://doi.org/10.1016/j.addma.2020.101750.
[18] D. Hoskins, V. Kunc, A. Hassen, J. Lindahl, C. Duty, Characterizing Thermal Expansion of Large-scale 3D Printed Parts, in: SAMPE 2019 - Charlotte NC, SAMPE, 2019. https://doi.org/10.33599/nasampe/s.19.1598.
[19] D. Hoskins, S. Kim, A. Hassen, J. Lindahl, V. Kunc, C. Duty, MODELING THERMAL EXPANSION OF A LARGE AREA EXTRUSION DEPOSITION ADDITIVELY MANUFACTURED PARTS USING A NON-HOMOGENIZED APPROACH, (n.d.) 10.
[20] P. Bing, X. Hui-min, H. Tao, A. Asundi, Measurement of coefficient of thermal expansion of films using digital image correlation method, Polym. Test. 28 (2009) 75–83. https://doi.org/10.1016/j.polymertesting.2008.11.004.
[21] T.C. Chu, W.F. Ranson, M.A. Sutton, Applications of digital-image-correlation techniques to experimental mechanics, Exp. Mech. 25 (1985) 232–244. https://doi.org/10.1007/BF02325092.
[22] J.S. Lyons, J. Liu, M.A. Sutton, High-temperature deformation measurements using digital-image correlation, Exp. Mech. 36 (1996) 64–70. https://doi.org/10.1007/BF02328699.
[23] B. Pan, K. Qian, H. Xie, A. Asundi, Two-dimensional digital image correlation for in-plane displacement and strain measurement: a review, Meas. Sci. Technol. 20 (2009) 062001. https://doi.org/10.1088/0957-0233/20/6/062001.
[24] B. Pan, H. Xie, Z. Wang, K. Qian, Z. Wang, Study on subset size selection in digital image correlation for speckle patterns, Opt. Express. 16 (2008) 7037. https://doi.org/10.1364/OE.16.007037.
[25] Workshop: DIC Overview of Principles and Software_Correlated Solutions_University of South Carolina_2009, (n.d.).
[26] S. Yaofeng, J.H.L. Pang, Study of optimal subset size in digital image correlation of speckle pattern images, Opt. Lasers Eng. 45 (2007) 967–974. https://doi.org/10.1016/j.optlaseng.2007.01.012.
[27] E37 Committee, Test Method for Length Change Calibration of Thermomechanical Analyzers, ASTM International, n.d. https://doi.org/10.1520/E2113-18.